01 Jan 2023

Point Density for Soil Specimen Volume Measurements in Image-Based Methods during Triaxial Testing

Sara Fayek

Xiong Zhang
Missouri University of Science and Technology, zhangxi@mst.edu

Javad Galinmoghadam

Jeffrey D. Cawlfield
Missouri University of Science and Technology, jdc@mst.edu

Recommended Citation

RESEARCH PAPER

Point density for soil specimen volume measurements in image-based methods during triaxial testing

Sara Fayek[1] · Xiong Zhang[1] (ORCID) · Javad Galinmoghadam[1] · Jeffrey Cawlfield[2]

This is a U.S. Government work and not under copyright protection in the US; foreign copyright protection may apply 2023

Abstract

Discrete measurement targets were frequently utilized in image-based methods on the specimen's surface to monitor the soil specimen during triaxial testing. However, the required density of measurement targets that should be used in triaxial testing to achieve highly accurate volume measurement has not been investigated. To overcome this limitation, this paper presents a parametric study to determine the optimum target/point densities to be utilized on the triaxial soil specimen surface to achieve the desired level of volume measurement accuracy in image-based methods. LiDAR scanning was applied to establish the "ground truth" volume of the specimen. The effects of deformation and failure modes were investigated by calculating the volume measurement accuracy at different strain levels and for different undisturbed soil specimens of clay and sand with silt. An interpolation method was proposed to increase the number of discrete targets representing the triaxial specimen's surface. The analysis results show that a higher target density is required at a larger strain. Also, adding the number of interpolation points can only increase the accuracy to a certain level. As the volume measurement accuracy was different for each of the clay and sand with silt specimens, the non-uniform deformation, and failure mode of the specimen can affect the required optimum density of discrete measurement targets. In conclusion, it is recommended to choose the optimum density of targets based on the accuracy requirement, the maximum soil deformation level, and the expected failure mode of the specimen.

Keywords Image-based method · LiDAR · Triaxial testing · Volume measurement

1 Introduction

In recent years, due to the increasing availability of inexpensive digital cameras, and the recent advancements in image analysis and computer vision, image-based techniques have been increasingly used in triaxial soil testing. Image-based methods have the advantage of obtaining full-field displacement measurements of the triaxial specimen at a low cost. By enabling the full-field displacement measurements, the behavior of both saturated and unsaturated soils during triaxial tests can further be evaluated by calculating one or more of the following: (1) total, local, and absolute volume [4, 26]; (2) axial and radial deformation at any location of the soil specimen at different testing time; (3) strain and volumetric strain measurements; and (4) shear band characterization (shear band thickness, formation, and propagation) [2–4, 8, 13, 14, 17, 19, 20, 26].

The three-dimensional (3D) reconstruction of the soil specimen is created by extracting qualitative information from analyzing the captured images of the specimen during triaxial testing. The 3D reconstruction of the specimen's surface is represented in the form of a "point cloud" which is a dataset composed of points located in a 3D coordinate space. Generally, the point cloud representing the soil specimen can be created in two ways: dense surface modeling and discrete measurement target marking. The dense surface modeling technique is based on the intricate features and patterns in processing the images and then

✉ Xiong Zhang
  zhangxi@mst.edu

1 Civil, Architectural and Environmental Engineering,
   Missouri University of Science and Technology, Rolla,
   MO 65409-0030, USA

2 Geosciences, Geological, and Petroleum Engineering,
   Missouri University of Science and Technology, Rolla,
   MO 65409-0030, USA

providing fully automatic matching between the points. Dense surface modeling normally requires that the specimen surface has a very good texture (contrasting image features) to get good matching points. In general, more points on the membrane can be detected using the dense surface modeling technique. However, it is extremely difficult, if not impossible, to match the same points in different images to the pixel level of accuracy. As the accuracy of this technique is dependent upon the physical area represented by each pixel, medium-density point clouds are mostly expected. Mismatching and mis-referencing the corresponding points in different pictures can result in inevitable noisy points which can reduce the robustness and accuracy of the dense surface analysis results. In addition, dense surface analysis involves a longer processing time for referencing and matching many points for surface characterization. The second method to represent the triaxial specimen's surface is the discrete measurement target marking. The discrete measurement targets can be automatically detected in the captured images during the image analyses. Instead of examining every pixel of images for feature matching, this method often calculates the centroid of each measurement target, which is a mathematical point without physical dimension [24]. As a result, the discrete measurement target marking can achieve a subpixel level of accuracy. Hence, all targets are identified in each image, the referencing and matching process is highly efficient and accurate. As far as processing goes, discrete measurement targets are treated like any other subpixel marked point which improves the speed of processing time [9].

Considering these advantages, many image-based methods in triaxial testing used different discrete measurement targets, as shown in Fig. 1, to reconstruct the surface of the triaxial soil specimen. This includes the dots marked in a grid pattern where black-colored latex dots were pasted or printed on the surface of the membrane as shown in Fig. 1a [24, 27]. Another type of discrete measurement target is the node of a colored square grid imprinted on the surface of the specimen. The checkerboard pattern presented in Fig. 1b is an example of the colored square grid [3]. Similarly, the intersecting nodes of the square grid can be used as discrete measurement targets. For example, the square grid pattern printed on the membrane surface shown in Fig. 1c [1]. Another type of discrete measurement target is the coded target which is a special design pattern of target that can be assigned to a particular identification (ID) number. Figure 1d shows one common type of coded target which is the black-ringed automatically detected (RAD) coded target [23, 26]. Another method for discrete measurement targets is the pixel subset matching that is illustrated conceptually in Fig. 1e. Through the latex specimen membrane, the unique

heterogeneous coloring of the sand grains over the surface of the specimen represents distinctive entities that can be tracked during triaxial testing [17]. A summary of the image-based methods that used different types of discrete targets is presented in Table 1 including related information in terms of volume measurement, spacing of targets, accuracy, system setup, and specimen coverage. These methods can be classified in terms of measurement principle, procedures, and system setup into three board categories: (1) digital image analysis [1, 2, 8, 13–15, 19, 22], (2) digital image correlation [3, 17, 18, 23], and (3) photogrammetric methods [5, 6, 20, 26].

However, the discrete measurement targets can occupy a larger area with a greater number of pixels in the pictures, which means fewer points can be used to represent the soil specimen's surface. In fact, the number of discrete measurement points can limit the mesh refinement of the triaxial soil specimen's surface. To have a better representation of the soil specimen, interpolation is often used to obtain more points on the soil surface. For example, the mesh generation of the soil specimen, shown in Fig. 2a, having a diameter of 71 and 140 mm in height can be presented in different ways depending on the number of measurement points considered on the specimen's surface. Figure 2b presents the soil specimen with 204 measurement targets on its surface. It can be noticed that generating the surface mesh using this number of targets is not the best way to represent the soil specimen surface. After applying surface interpolation, 49,500 points were used to create the mesh of the specimen's surface. It can be noticed from Fig. 2c, that the generated mesh using a higher number of points can better represent the soil specimen. So, surface interpolation can be used to get a better representation of the soil specimen. In fact, interpolation is also needed for the dense surface point clouds since the surface measurement is not continuous considering that each pixel represents a physical area, and pixel-by-pixel level accuracy cannot be accomplished. Also, it is commonly noticed that some parts of the scanned object might be missing in the dense surface model due to accessibility reasons, reflection problems, unreliable marking, and mis-referencing difficulties [16]. In a summary, both dense surface modeling and discrete measurement target marking are considered discrete measurement techniques that might require surface interpolation for a better representation of the soil specimen.

As the discrete measurement target marking has high accuracy and robustness with little chance of unreliable marking and mis-references points, it is preferable to use discrete measurement targets to represent the triaxial soil specimen. However, the limited number of discrete targets that can be used is the major drawback of this method in triaxial testing. For example, Salazar and Coffman [21]
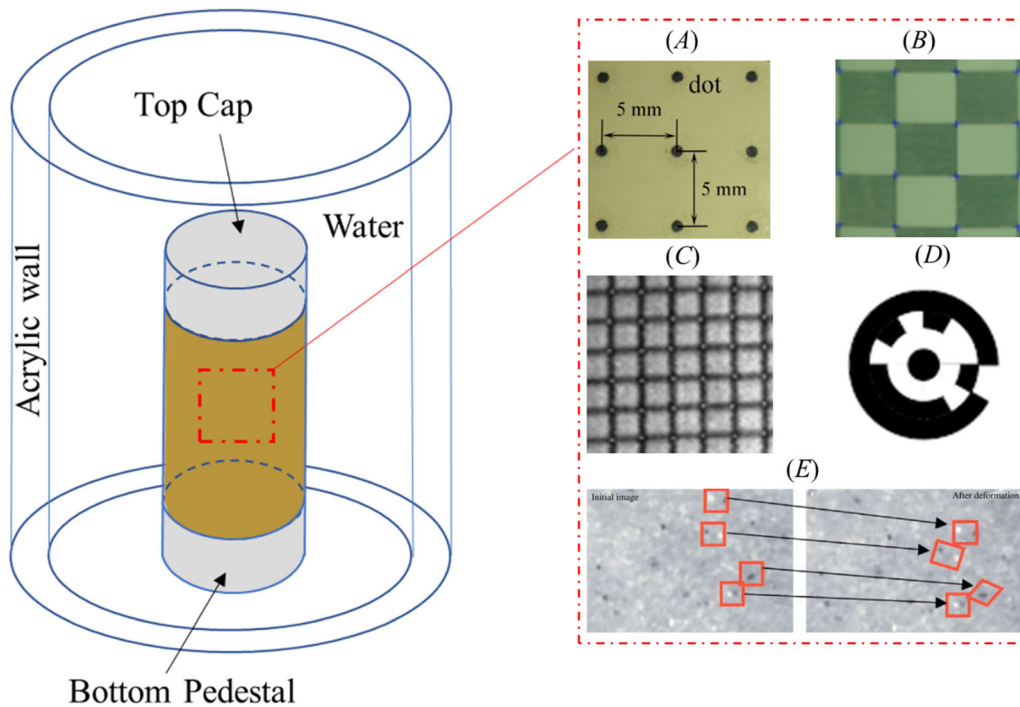
Fig. 1 Different measurement targets used in triaxial testing: **a** dots marked in a grid pattern (from Zhao and Koseki [27]), **b** nodes of a colored square grid (from Bhandari et al. [3]), **c** intersecting points of the square grid (from Alshibli and Sture [1]) **d** coded target (from Zhang et al. [26]), and **e** pixel subset matching (modified from Rechenmacher and Medina-Cetina [18])

questioned the effect of the number of measurement points on the accuracy of the local and total volume results presented in Zhang et al. [26]. This concern is valid for all image-based methods that utilized discrete measurement targets. Then the question remained unanswered: How many targets are needed for an accurate representation of a soil specimen? Since soil specimens can have different dimensions, the actual question is: What is the required target density per surface area to better represent the triaxial soil specimen and to achieve high measurement accuracy?

To answer this question, this paper attempts to examine the effect of the discrete targets' density on the measurement accuracy in image-based methods during triaxial testing. In this study, the discussion is focused on volume measurements of the triaxial soil specimen. To evaluate the effect of the discrete targets' density on the volume measurement of the triaxial soil specimen, different densities of discrete targets were considered to represent the soil specimen's surface. The reference volume of the soil specimen was determined using the 3D terrestrial light detection and ranging (LiDAR) scanner (Leica 736 ScanStation P40). The LiDAR scanner uses a pulsed laser to calculate the distance between the sensor and the target object; then, the information collected by the scanner was put together to generate a precise 3D dense point cloud of the object. However, the laser points emitted to the acrylic

wall and water can cause usage limitations associated with refractions and light absorption [25]. To eliminate these drawbacks, unconfined compression tests were performed to simulate specimen deformation similar to those during triaxial testing. Two undisturbed specimens of clay and sand with silt were tested independently to determine the influence of deformation patterns and failure modes associated with different soil types on the volume measurement accuracy. The soil specimens were scanned at different stages during the unconfined compression test to investigate the effect of the specimen's deformed shape in relation to different strain levels on the volume measurement accuracy. A surface interpolation was proposed and used to ensure a better representation of the soil specimen. The comparison between the reference volume and that of the specimen reconstructed from different densities of measurement targets is used to calculate the volume measurement accuracy at different strain levels for each soil specimen.

2 Research methodology

The objective of this study is to determine the discrete target density requirement on the specimen's surface to achieve highly accurate volume measurement during triaxial testing. The accuracy of volume measurements was

Table 1 Different types of measurement targets used in triaxial testing in various image-based methods

Type of measurement targets	References	Method	Volume measurement	Spacing (center to center)	Accuracy	Specimen coverage	System Setup
Dots marked in a grid pattern (Fig. 1a)	Kikkawa et al. [11]	Stereo photogrammetry	Total and local	10° intervals in the circumferential direction and 5 mm intervals in the vertical direction	Accuracy of 0.1 pixel	360° coverage of the specimen	Eight digital cameras were set around the circumference of the triaxial cell at 45° intervals
	Lin and Penumadu [13]	Digital image analysis with refraction correction	Local	Approximately 10 mm spacing	Accuracy of measurement of 0.2 mm in the vertical direction and 0.3 mm in the circumferential direction	10 cm × 20 cm zone of measurement, which is equivalent to a 102 degree	One digital camera was mounted outside the triaxial cell
	Sachan and Penumadu [19]	Digital image analysis with refraction correction	Local	Approximately 10 mm spacing	The point measurement accuracy was reported to be 0.2 and 0.3 mm in the vertical and circumferential directions, respectively; the measurement error can yield a ± 2%; 0.2 mm tolerance in a vertical direction	10 cm × 10 cm zone of measurement, which is equivalent to a 102 degree	One digital camera was mounted on a two-axis controller, which allowed for precisely adjusting the camera position in two directions
	Li et al. [12]	The photogrammetry-based method with a refraction correction	Total and local	A 1.3 mm between dots	The value of accuracy is not mentioned	360° coverage	Six cameras were mounted outside the triaxial cell
Intersecting points of the colored square grid (Fig. 1b)	Bhandari et al. [3]	Digital image correlation	Total and local	A grid spacing is 10 mm	The difference between the image-based and the LVDT measurements was found to be better than 0.10 pixels (or 0.004 mm in the object space at a nominal image scale of 0.04 mm/pixel at the center of the image)	360° coverage	Three digital cameras (SONY DSC-R1 Cyber-shot 10 megapixels) were placed outside the transparent triaxial cell on radii 120° apart
Intersecting points of the square grid (Fig. 1c)	Alshibli and Sture [1]	Digital imaging analysis	Local	5 mm by 5 mm	The error of 0.18 mm and 0.28 mm for the shear band measurement	7 cm × 15 cm zone of measurement, which is equivalent to 102 degree	A video camera was used to monitor the specimen outside the triaxial cell
	Alshibli and Alhamdan [2]	Digital imaging analysis	Total and local	30 grid lines along with the height of the specimen (h = 150 mm). The spacing is approximately 5 mm	The value of accuracy is not mentioned	360° coverage of the specimen	Three CCD cameras and a recorder

Table 1 (continued)

| Type of measurement targets	References	Method	Volume measurement	Spacing (center to center)	Accuracy	Specimen coverage	System Setup
Ringed automatically detected (RAD) coded targets (Fig. 1d)	Zhang et al. [26]	The photogrammetry-based method with a refraction correction	Total and local	16 targets in the vertical dimension and 21 targets in the circumferential dimension. The diameter and height of the specimen are 71 and 137 mm	The average accuracy for a single target ranges from 0.056 to 0.076. The accuracy for total volume measurement is better than 0.25%	360° coverage of the specimen	A single digital camera placed outside the triaxial cell
	Salazar et al. [20]	Internal photogrammetry-based method	Total and local	286 targets adhered to the membrane. Specimen is 38.1 mm [1.5 in] diameter by 76.2 mm [3.0 in] height	The volume measurement error ranged from 0.13 to 0.5%	360° coverage of the specimen	10 customized pinhole cameras placed inside the triaxial cell
	Fayek et al. [4]	The photogrammetry-based method with a refraction correction	Total, local, and absolute	234 targets adhered to the membrane. The specimen is 70 mm in diameter by 149 mm in height	The accuracy for total volume measurement is better than 0.061%	360° coverage of the specimen	A single digital camera placed outside the triaxial cell
Pixel subset matching (Fig. 1e)	Rechenmacher and Medina-Cetina [18]	Three-dimensional digital image correlation	Local	Depends on the subset matching of soil	The accuracy of the vertical displacement could be ± 0.02 mm	85° coverage of the specimen	Two digital cameras with an experimental-grade charge-coupled device (CCD)
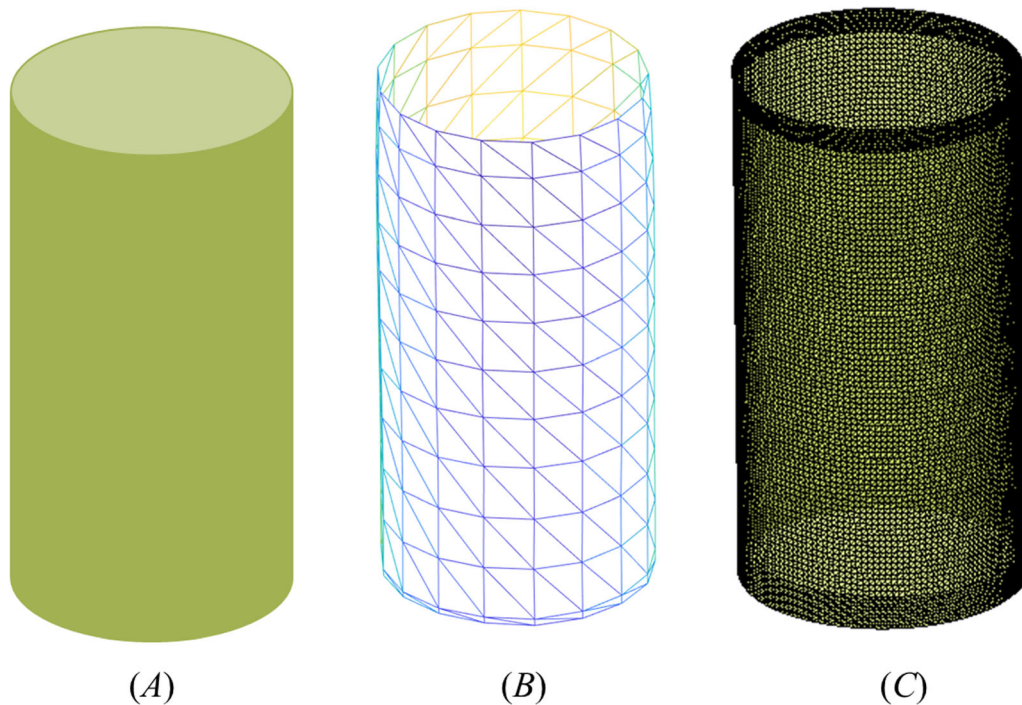
Fig. 2 Influence of the number of targets on the surface shape of soil specimen: **a** a cylindrical soil specimen, **b** mesh formed with 204 targets, and **c** mesh formed with 45,900 targets

determined by comparing the ground truth reference volume of the specimen to the specimen's volume corresponding to different target densities at the specimen's surface. The LiDAR scanner was used to determine the ground truth reference volume of the soil specimen. LiDAR scanner is a highly effective method for collecting massive volumes of precise and high-resolution information for 3D reconstruction [9, 10] where an angular accuracy is $(8/3600)°$, a linear accuracy is 0.013 mm, and a 3D position accuracy is 0.18 mm for the range used in this research, based on the scanner user manual. It is worth noting that the accuracy of the LiDAR scanner was validated by scanning a stainless steel specimen with known dimensions. A comparison between the volume for a stainless steel cylinder and that determined from the LiDAR scanner showed an accuracy higher than 99.99%. This accuracy was calculated as the average of the volume measurement accuracy for repeatable validation tests on the cylinder. Cleaning and removing noise from the 3D point cloud was applied using MATLAB. It is worth noting that the 3D position error of individual points in the point cloud caused the points to move near or far from the center of the cylinder which might be a factor in achieving this high-volume measurement accuracy.

To eliminate the refraction effect at the air–acrylic and acrylic–water interfaces, unconfining compression tests were performed instead of triaxial testing. However, the conclusion of this research can be applied to both unconfined compression tests and triaxial tests. The methodology proposed in this research is shown in the diagram presented in Fig. 3 and involves three main steps: (1) preprocessing, preparing an undisturbed soil specimen with a diameter of 71 mm and a height of 140 mm, then covering the specimen with a latex membrane and posting black circular measurement targets on the membrane surface. The black measurement targets were used so that their centroids can be accurately determined and tracked during testing, and to facilitate the discussions and comparison with discrete measurement targets that are usually used in image-based methods. Since the clay and sand with silt specimens have different deformation patterns that can influence the volume measurement accuracy, two representative specimens of sand with silt and clay were used to demonstrate the impact of different soil types on the point density requirements. Additional targets were placed on the periphery and surface of each of the top cap and bottom pedestal to be used to back-calculate the specimen ends by applying Fayek et al. [4]'s proposed method; (2) processing, performing an unconfined compression test for each specimen. The specimen was scanned at the start of the test using the LiDAR scanner, at an interval of 3% until 15% strain, from three different positions (120° apart) to ensure 360° specimen coverage. Then, the scans were assembled to create a 3D dense surface model of the specimen at each
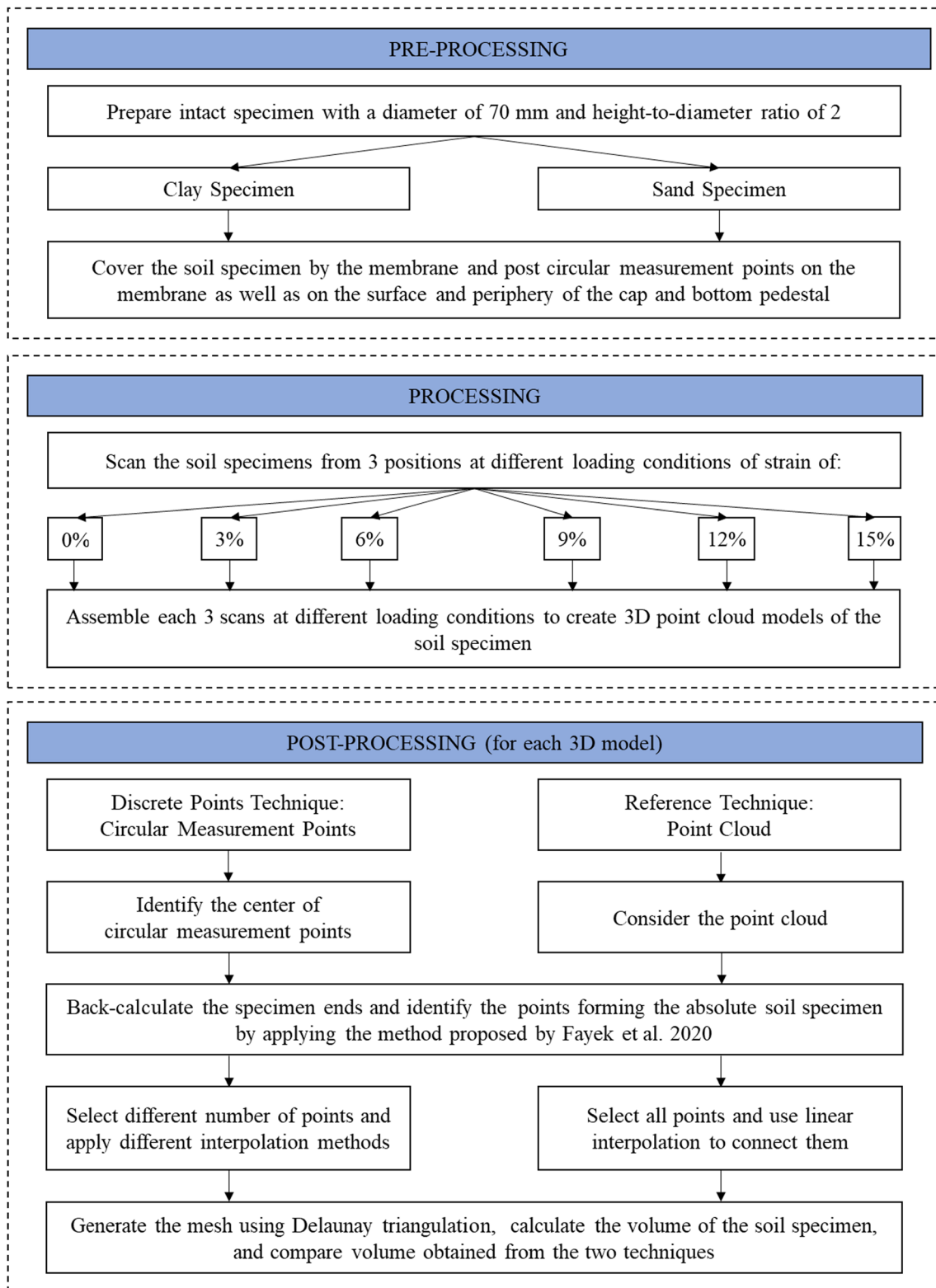
Fig. 3 Flowchart of the methodology proposed

strain level; and (3) post-processing, the entire point cloud was first considered; then, the centroids of the discrete targets were selected from the point cloud to mark the

position and coordinates of the discrete targets. For both methods, the specimen ends were back-calculated and the points between the two ends were used to determine the

absolute soil specimen [4]. Different interpolation methods were applied to form a 3D surface from the discrete points while simple linear interpolation was used to connect the dense point cloud. Delaunay triangulation was used for both methods to generate a mesh of the soil specimen. Then the volume of the soil specimen was calculated for both methods, and the two calculated volumes were compared to determine the accuracy associated with different target densities.

3 Experimental program and setup

3.1 System setup and tested material

The unconfined compression tests were performed on two undisturbed specimens of clay and sand with silt. The undisturbed sand specimen containing silt contents was classified as well-graded sand with silt (SW-SM), and the clay specimen was classified as lean clay (CL). The two specimens were extracted from two undisturbed Shelby tube samples obtained from an excavation pit in Missouri. Then, the specimens were trimmed carefully to a diameter of 71 mm and a height of 140 mm. The surfaces of the specimens' ends were polished to be flat, vertical, and parallel to ensure that the specimen ends are perpendicular to the longitudinal axis of the specimen.

The experimental test setup is presented in Fig. 4a comprising the testing apparatus, the soil specimen, the measurement targets, and the LiDAR scanner. Unconfined compression test apparatus with a deformation indicator was used to apply the axial load to the soil specimen. The specimen was placed in the unconfined compression test apparatus centered on the bottom pedestal. After the latex membrane was placed to cover the soil specimen, the loading device was carefully adjusted so the top cap just makes contact with the specimen. Then black circular discrete measurement targets were manually posted on the membrane's external surface at an equal interval of 1 cm on the vertical axis and the circumferential axis (Fig. 4a). The unique texture of these matt black circular targets allows them to be easily detected after scanning. Additional targets were placed on the surface plan and periphery for each of the top cap and bottom pedestal as shown in Fig. 4b, c, respectively. The targets on the top cap and bottom pedestal were used to back-calculate the specimen ends during testing by applying the method proposed by Fayek et al. [4, 7]. The LiDAR scanner was utilized to reconstruct a 3D colored model of the soil specimen at different strain levels until reaching 15% strain. The 3D scanning involved placing the LiDAR scanner at a 3 m distance from the soil specimen at three different positions, 120° apart, to ensure full coverage of the soil specimen (Fig. 4a).

Since these two specimens are expected to have different failure modes, the deformed shapes for both specimens during testing and at failure are distinct (Fig. 5). Although both specimens have the same undeformed shape at 0%
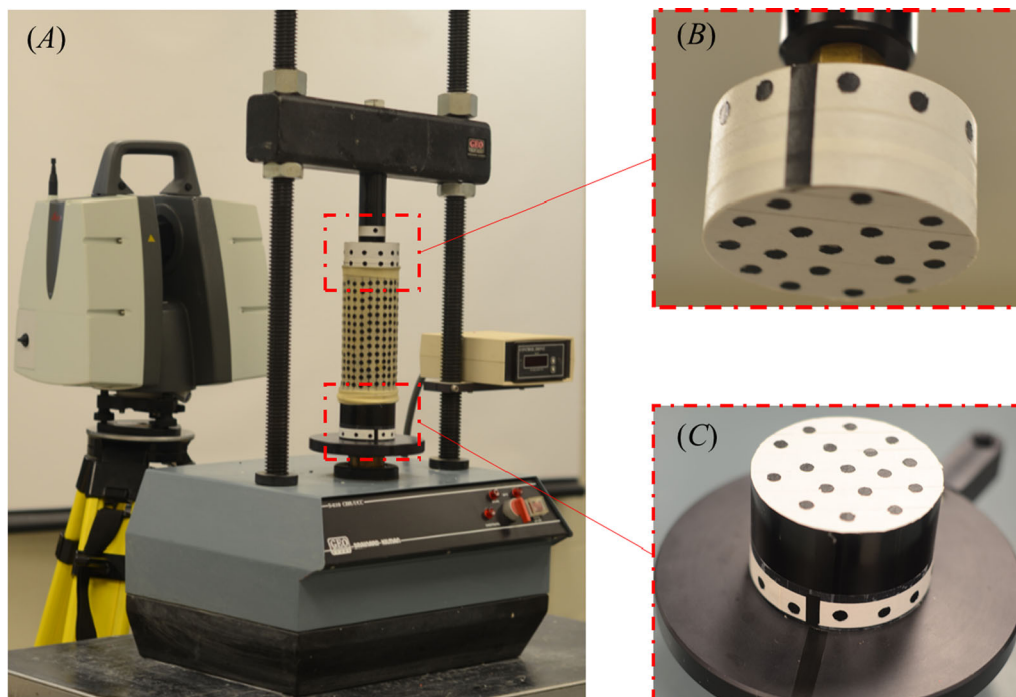

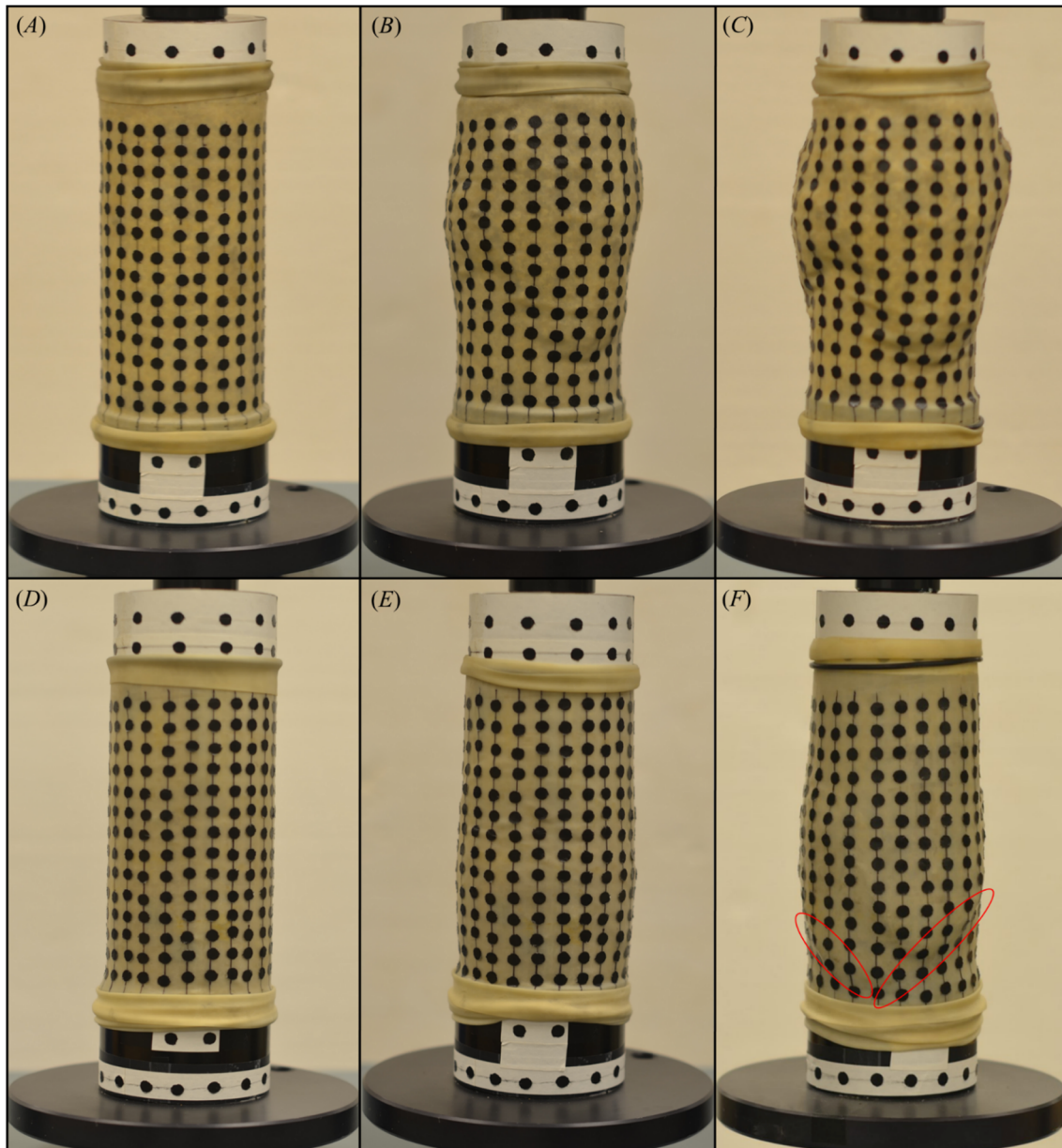Fig. 4 a System setup, b top cap, and c bottom pedestal

Fig. 5 Deformation at different strain levels for two different specimens: **a** sand specimen at 0% strain, **b** sand specimen at 9% strain, **c** sand specimen at 15% strain, **d** clay specimen at 0% strain, **e** clay specimen at 9% strain, and **f** clay specimen at 15% strain

strain as shown in Fig. 5a, d, the shape of each specimen started to diverge with increasing the strain level (Figs. 5b, e). In addition to that, the failure mode of the sand specimen presented in Fig. 5c shows bulging failure at 15% strain with a general deformation across the specimen. However, the failure mode of the clay specimen presented in Fig. 5f showed localized failure mode by shear band formation. Since the deformed shapes of each specimen are very different, it is critical to consider both specimens for examining the effect of soil type on the required target density on the specimen's surface.

3.2 Dense surface modeling

In this section, the workflow used in determining the reference point cloud of the specimen generated from the 3D scanning is described. A 3D scanner utilizing LiDAR technology and a computer imaging program were used to reconstruct a colored 3D point cloud of the soil specimen. In addition, the onboard camera of the LiDAR scanner captured images of the soil specimen at each scan position. Figure 6a shows a picture of the soil specimen during the unconfined compression test captured by the onboard camera of the LiDAR scanner. Then, the processing unit
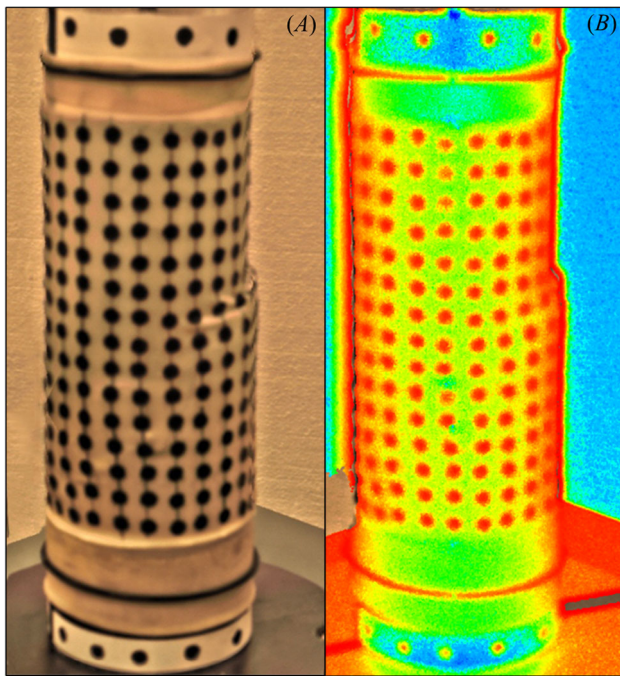
Fig. 6 a A captured picture for the soil specimen "A" by the onboard camera of the LiDAR and **b** a scan of the soil specimen by the LiDAR showing distinct colors

highlights the pixel contingent on the change of light density where different colors are presented as shown in Fig. 6b. In Fig. 6b, the red pixels of the image, which are identified on the specimen's surface and the peripheral surface of both the top cap and bottom pedestal, are the circular measurement targets. Using the developed post-processing MATLAB program, each target was identified separately by a group of red points. Since the target has a circular shape, the center of each target has been identified by determining the centroid of the group of red points. The exact location and coordinates of these centroids were saved to be used in the analysis at each strain level. A similar procedure was applied to both the top cap and bottom pedestal before initiating the test. Each of the top cap and the bottom pedestal, shown in Fig. 4b, c, respectively, were scanned individually from three different positions by the LiDAR scanner. The unique texture of the targets placed on the surface and periphery of the pedestals allows targets to be easily detected. After scanning, these targets are identified by red color. Then, the pixels corresponding to the centers of these targets were determined and assigned to given numbers. The 3D coordinates of the centers of the targets on the top surface and those on the periphery were saved separately. Using the 3D coordinates of the center of the targets placed on the surface of each of the top cap and bottom pedestal, the plane equation of each surface was calculated by applying a least-square optimization process. Once the location of the surface plane of

each pedestal was determined, the distances from each target placed on the periphery to the surface plane were calculated. These distances were saved to be used in the subsequent steps to back-calculate the specimen's ends during the unconfined compression test.

To obtain a complete 3D point cloud with full coverage of the soil specimen, three scans from different positions of the specimen at each strain level are required. This procedure is repeated during the unconfined compression test by scanning the specimen starting at 0% until 15% strain with an interval of 3%. After scanning is complete, the three scans corresponding to each strain level were assembled using a commercial software to create a 3D point cloud of the soil specimen. Then, the 3D point cloud was further edited by removing noisy points. This included trimming any background details that may have been scanned unintentionally. This is followed by trimming unnecessary points of the apparatus above the top cap and below the bottom pedestal.

By using the calculated distances from the peripheral targets on each of the top cap and bottom pedestal to its surfaces, the planes representing the specimen ends can be back-calculated. A MATLAB program was developed to perform the post-processing operations. The points corresponding to the absolute soil specimen were automatically identified between the top and bottom planes. Then, a mesh was generated by connecting linearly all points forming the absolute soil specimen using Delaunay triangulation. Although there are many algorithms for computing triangulations, it is the favorable geometric properties of the Delaunay triangulation which make it very valuable. The Delaunay triangulations have important implications in practice and motivate the use of Delaunay triangulations in scattered data interpolation due to two main characteristics: (1) the nearest-neighbor relation. The Delaunay triangulation connects points in a nearest-neighbor manner; (2) the well-shaped triangles. The fundamental property of the Delaunay triangulations is the Delaunay criterion. The Delaunay triangulation of the points ensures the circumcircle associated with each triangle contains no other point in its interior. So that, Delaunay triangles are "well shaped" because in fulfilling the empty circumcircle property, triangles with large internal angles are selected over ones with small internal angles. The "Delaunay triangulation" function in MATLAB was used to generate the mesh of the cylinder. This function takes a set of points and produce a triangulation in matrix format. The produced triangulations were then used to plot a surface defined in terms of a set of scattered data points. An arbitrary point C was added in the center of the enclosed mesh, then connected with all triangles of the latest formed enclosed mesh. By connecting this center point with every three vertices (P_{1t}, P_{2t} and P_{3t}) of the triangular mesh, a series of

tetrahedrons was formed. The soil specimen volume was then determined by summing all tetrahedrons' volumes, which is calculated given the 4 vertices (C, P_{1t}, P_{2t} and P_{3t}) of each tetrahedron using Eq. (1) as follows:

$$V = \sum_{t=1}^{T} v_t = \frac{1}{6} \sum_{t=1}^{T} \left| \overrightarrow{CP_{1t}} \cdot \left(\overrightarrow{CP_{2t}} x \overrightarrow{CP_{3t}} \right) \right| \tag{1}$$

where t is the ordering number of tetrahedrons of the total T tetrahedrons.

3.3 Discrete measurement targets marking

The discrete measurement target marking is performed by identifying the centroid and location of the targets in the point cloud. Based on the difference in light intensity acquired from the scanner, all discrete targets were flagged with a red color. Three different values of measurement target's density were considered based on selecting different numbers of targets at different spacing as follows: (1) The centroids of the red circles corresponding to the discrete targets were selected which resulted in discrete targets with an approximate spacing of 1 cm that is equivalent to 114 targets/100 cm^2 of the specimen's surface; (2) the midpoints between precedent targets were selected from the point cloud in addition to the centroid of targets which resulted in discrete targets with an approximate spacing of 0.5 cm that is equivalent to 456 targets/ 100 cm^2 of the specimen's surface; and (3) the centroids of the targets were selected by considering only half the numbers of columns and rows which resulted in 2 cm spacing between targets that is equivalent to approximately 29 targets/100 cm^2 of the specimen's surface. Each model of the three above is considered separately to investigate the effect of target density on the accuracy of volume measurement. For each model, the top and bottom specimen's ends were back-calculated by applying the method proposed by Fayek et al. [4]. Then the absolute soil specimen was determined based on the points bounded by the top and bottom planes. To ensure a better representation of soil specimens and accurate volume calculation, a cylindrical surface interpolation method was proposed that allows a better representation of the soil specimen. This cylindrical surface interpolation increases the number of points on the specimen's surface that is proficient to determine an accurate and representative volume of the soil specimen. First, the Cartesian coordinate systems (x, y, z) of all points cloud were transformed into 3D polar coordinates of r, θ, and h (r is the radius, θ is the angle, and h is the height of the point). Next, an interpolation between every two consecutive points in each row and column of the cylinder was applied using Eqs. (2), (3), and (4) as follows:

$$r_{(ijk)n} = r_{ij} + \frac{k\left(r_{ij} + r_{i(j+1)}\right)}{m+1} \tag{2}$$

$$\theta_{(ijk)n} = \theta_{ij} + \frac{k\left(\theta_{ij} + \theta_{i(j+1)}\right)}{m+1} \tag{3}$$

$$h_{(ijk)n} = h_{ij} + \frac{k\left(h_{ij} + h_{i(j+1)}\right)}{m+1} \tag{4}$$

where i is the row ordering number, j is the column ordering number, k is the ordering number of interpolation points, and m is the total number of interpolation points between two consequent measurement targets.

The curvature surface interpolation of the specimen was applied by using different numbers of interpolation points "m" starting from $m = 0$ which is equivalent to linear interpolation till $m = 20$ at an interval of 1. By using a higher value of "m," the number of points representing the soil specimen is highly increased. After applying the surface interpolation at different values of "m," the mesh was generated for the specimen surface considering all points. Then the volume of the mesh is calculated using Eq. (1).

4 Results and discussions

The effect of the density of targets adhered to the specimen's surface on the volume measurement was investigated for image-based methods during triaxial testing. The LiDAR scanner was used to obtain the reference "true" volume of the soil specimen. To avoid refraction distortion during triaxial testing, unconfined compression tests were performed instead of triaxial testing. As mentioned previously, two different soil specimens were used to demonstrate the effect of the deformation and failure mode on the point density requirement. The reference specimen point cloud was obtained by assembling the different specimen scanning at each strain level to ensure full coverage of the specimen. An example of the point cloud of the sand specimen at 15% strain is shown in Fig. 7a. By applying the method proposed by Fayek et al. [4], the top and bottom planes representing the specimen's ends were back-calculated. Figure 7b shows the position of the top and bottom specimen's ends in the point cloud. Then, the points representing the absolute soil specimen were selected by only considering the points between the top and bottom planes and those intersecting the two planes. The absolute soil specimen and the specimen ends are shown in Fig. 7c. Since the point cloud is very dense, linear interpolation was applied to connect the point cloud. Delaunay triangulation was used to generate a mesh for the absolute soil specimen as presented in Fig. 7d. By considering the vertices and faces of the mesh, the reference volume of the soil, denoted
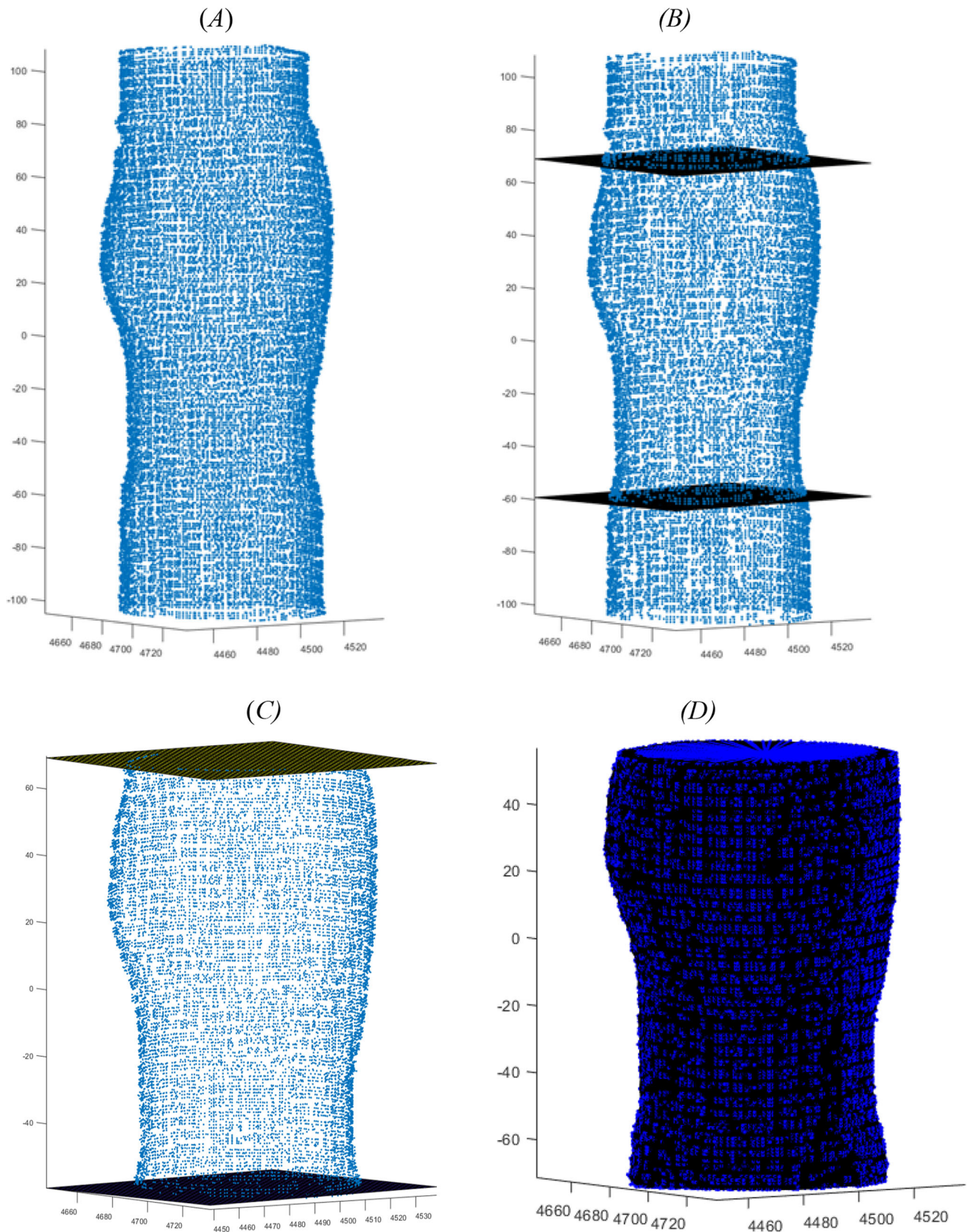
Fig. 7 **a** Points cloud of the sand specimen at 15% strain, **b** back-calculating of the top and bottom planes, **c** enclosed points between the top and bottom plane forming the absolute soil specimen, and **d** 3D mesh generation
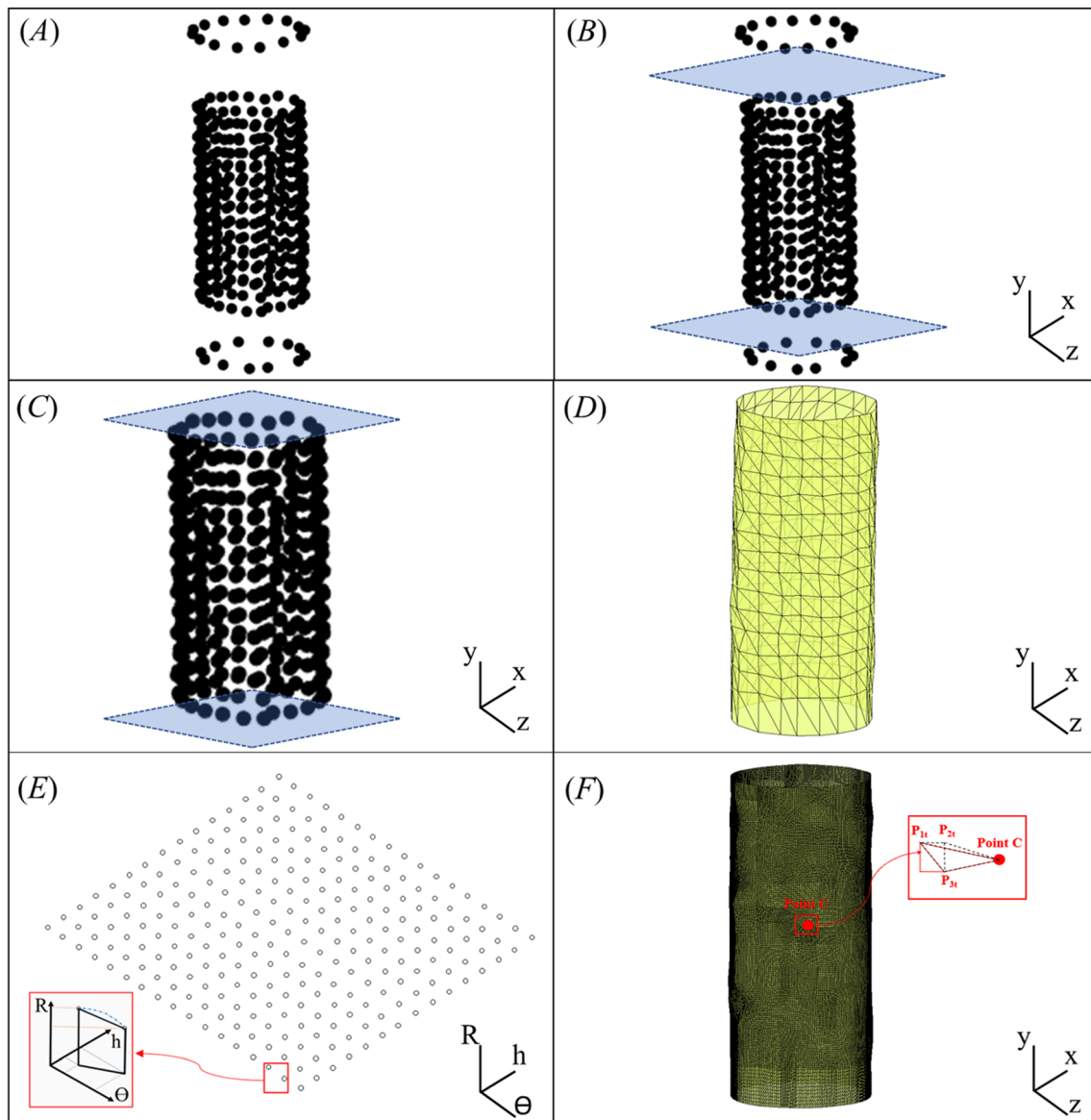
Fig. 8 **a** Points cloud of the clay specimen at 0% strain, **b** points cloud of the clay specimen with the top and bottom surfaces, **c** enclosed point cloud of the clay specimen with the top and bottom surfaces, **d** enclosed 3D mesh generation, **e** surface curvature interpolation, **f** new 3D mesh generation and specimen's volume calculation

by "V_s," where s is the strain level, was calculated using Eq. (1).

On the other hand, the centroids and positions of the discrete circular measurement points from the point cloud were selected based on their red colors. From the point cloud, the centroids of the measurement targets were identified. Then three different target groups were selected to consider 0.5, 1, and 2 cm spacing between targets. Figure 8a shows the targets with 1 cm spacing placed on the surface of the clay soil specimen at 0% strain. By considering the 3D coordinates of the targets on the periphery of the top cap and bottom pedestal, the specimen's ends were back-calculated as shown in Fig. 8b. Then

the points between the specimen ends were identified as the absolute soil specimen as shown in Fig. 8c. Linear interpolation was applied to connect these points where Delaunay triangulation was used to form a mesh of the soil specimen. It can be noticed that the mesh of the specimen presented in Fig. 8d is not the best representation of the soil specimen. So, the surface interpolation was applied by first transforming the 3D coordinates of the absolute specimen from the Cartesian coordinate system (x, y, z) into a 3D polar coordinate system (r, h, θ) as shown in Fig. 8e. The interpolation method, which was presented previously in Eqs. (2), (3), and (4), was applied considering different values of "m." After applying the interpolation

method, the points were transformed from a polar coordinate system to a Cartesian coordinate system. Then the mesh of the soil specimen was formed as shown in Fig. 8f. By selecting a point C in the center of the specimen, the absolute soil volume, denoted by "V_{sm}" where s is the strain level and m is the number of interpolation points, was calculated by applying Eq. (1).

The proposed cylindrical interpolation method was used to increase the number of points at the specimen's surface
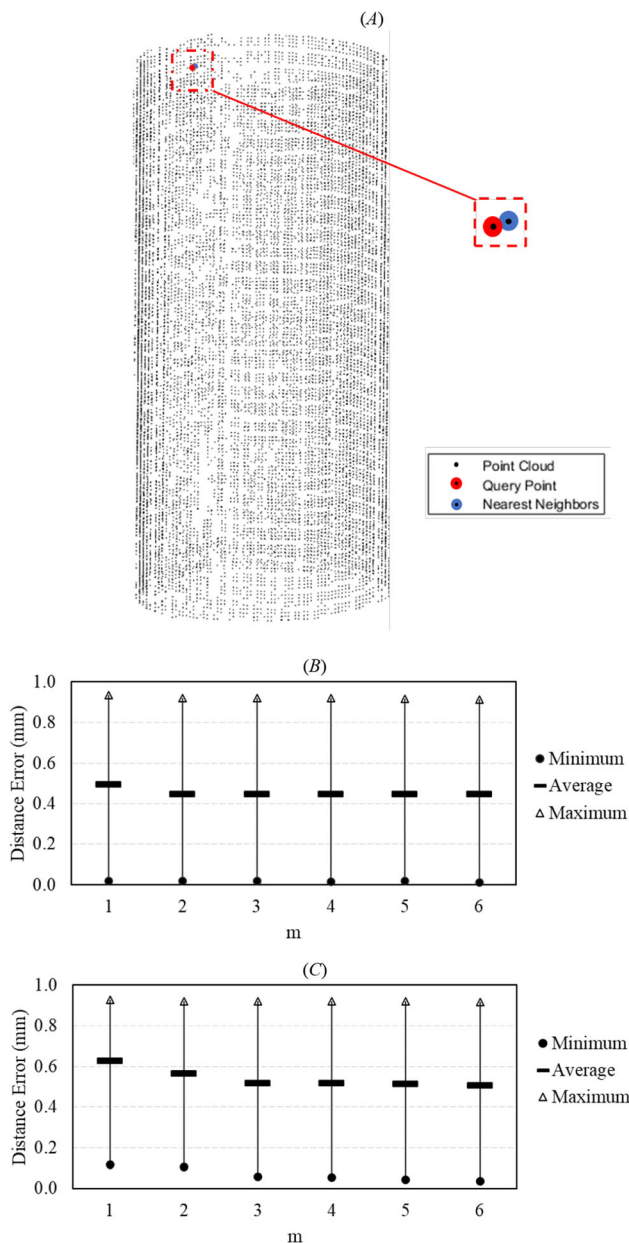

Fig. 9 a Soil specimen point cloud including the query point and its nearest neighbor, b distance error of the clay specimen at a different number of interpolation points at 0% strain, and c distance error of the clay specimen at a different number of interpolation points at 15% strain

to have a better representation of the specimen's shape and accordingly higher-volume measurement accuracy. However, the accuracy of the proposed cylindrical interpolation method needed to be investigated to determine the proximity of the new interpolated points to the real existing points in the reference dense point cloud. This was achieved by determining the K-nearest neighbors, with $K = 1$, of each new interpolated point in the point cloud by using the Kd-tree-based search algorithm. Figure 9 shows the distance errors between the new interpolated points to their nearest point in the dense point cloud for the clay specimen. Figure 9a shows the point cloud of the specimen in black where the query point is represented in red and its nearest neighbor in the point cloud in blue. It can be noticed that the query point and its corresponding neighbor are very contiguous. The distance errors of all query points and their corresponding neighbor are represented in terms of their maximum, mean, and minimum values at 0% strain and 15% strain in Fig. 9b, c, respectively. At 0% strain, it can be noticed that the mean distance error is around 0.5 mm at $m = 0$; then, it decreases to 0.45 mm at $m = 6$. In addition, the minimum distance error is around 0.01 mm at different interpolation points number. The maximum distance error is 0.92 mm at $m = 0$, and it decreases to approximately 0.9 mm at $m = 6$. The results of maximum, average, and minimum distance errors are very similar to those presented for the sand specimen at 0% strain since both specimens have an undeformed cylindrical shape at 0% strain. Figure 9c presents the error results at 15% strain and showed higher values of the average distance errors in comparison with those at 0% strain. This is associated with the increased non-uniform deformation of the soil specimen at 15% strain. The mean distance errors at 15% strain for the clay specimen showed higher values in comparison with those for the sand specimen which is related to the difference in the deformation shape between the two specimens. For example, the mean distance error at 15% strain for the clay specimen at $m = 6$ is 0.504 mm compared with 0.457 mm for the sand specimen at the same strain and m value. The maximum distance errors at different interpolation values are almost similar and equal to 0.91 mm. The minimum distance error is around 0.1 mm at $m = 1$ and then decreases to reach 0.03 mm at $m = 6$. The results shown in Fig. 9 proved the efficiency of the proposed interpolation method to approximate the locations of added points on the specimen's surface to be very close and realistic to the specimen's actual shape.

The volume calculation at different strain levels of each of the sand and clay specimens is presented in Fig. 10a, b, respectively. Then, the accuracy of the volume measurement using discrete points was calculated by dividing the absolute volume of the specimen formed by different numbers of targets "V_{sm}" with the reference volume
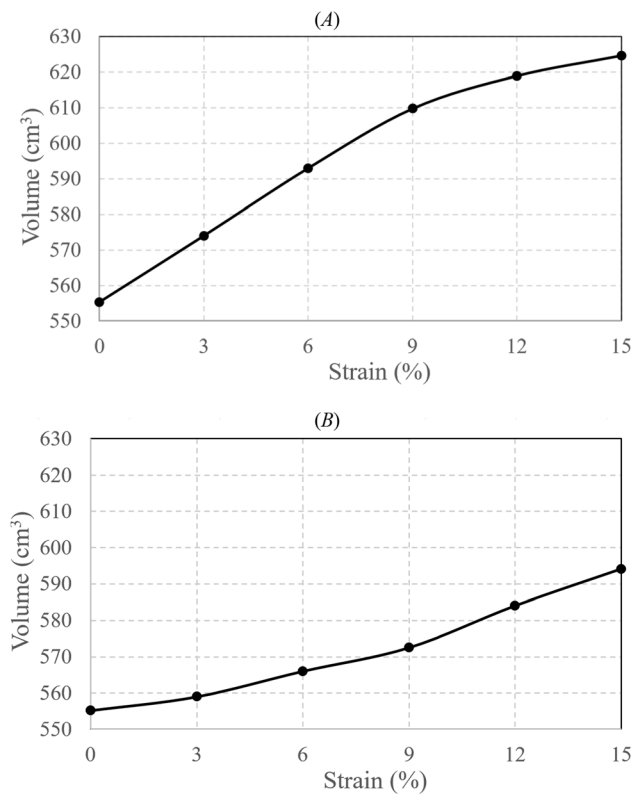
Fig. 10 Volume calculation at different strain levels for **a** the sand with silt specimen, **b** the clay specimen

considering all points cloud "V_s" (accuracy = V_{sm}/V_s). The accuracy was calculated at different strain levels using different interpolation targets for both sand with silt and clay specimens.

Figures 11 and 12 present the results of the unconfined compression test for the sand with silt and clay specimens, respectively, at different strain levels. The relationship is shown between volume measurement accuracy and the target density using different interpolation points. Figure 11a shows the variation of volume measurement accuracy at 0% strain with respect to interpolation points at different target densities. These results represent the initial condition of the soil specimen before the initiation of the test. At this strain level, the specimen's shape is similar to a perfect cylinder as shown in Fig. 5a and had a volume of $5.553*10^2$ cm^3 as shown in Fig. 10a. It can be noticed that the plots at different densities of 29 targets/100 cm^2, 114 targets/100 cm^2, and 456 targets/100 cm^2 showed similar trends. The results show higher accuracy values with the increasing number of interpolation points. The volume measurement accuracy shows a quick increase at the beginning of the application of the interpolation method and then a slow increase after adding a few interpolation points. As for using 29 targets/100 cm^2 on the membrane surface area, the accuracy presents a stiffer slope at the
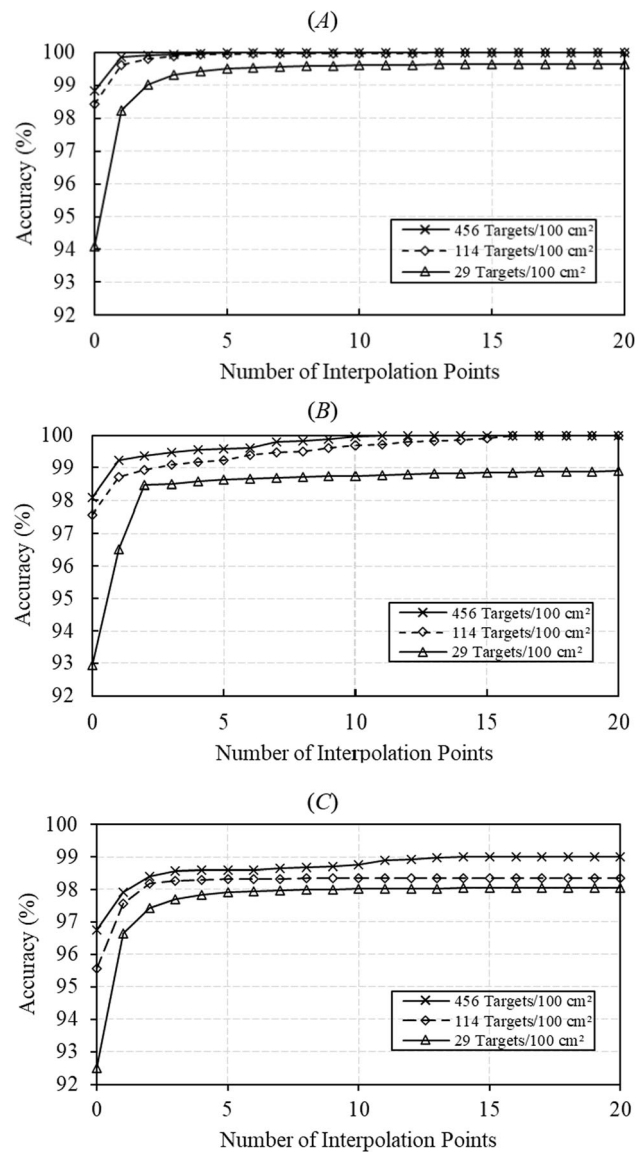

Fig. 11 Accuracy of volume calculation of the sand specimen at a different number of interpolation points at **a** 0% strain, **b** 9% strain, and **c** 15% strain

beginning of the application of the interpolation points, with an initial accuracy of 94% at 0 interpolation points (which is equivalent to linear interpolation) to 99% after applying the curvature surface interpolation with 3 points. Then the accuracy shows a steady accuracy of 99.4% after applying the interpolation with 7 points. As for using 114 targets/100 cm^2 on the membrane surface area, the accuracy quickly increases from 98.5 to 100% after 5 interpolation points. As for using 456 targets/100 cm^2 on the membrane surface area, the accuracy is almost steady after 3 interpolation points with a very high accuracy of 100%. It is worth noting that the initial accuracy corresponding to 0 interpolation point is highest for 456 targets/100 cm^2 followed by 114 targets/100 cm^2 then 29 targets/100 cm^2.
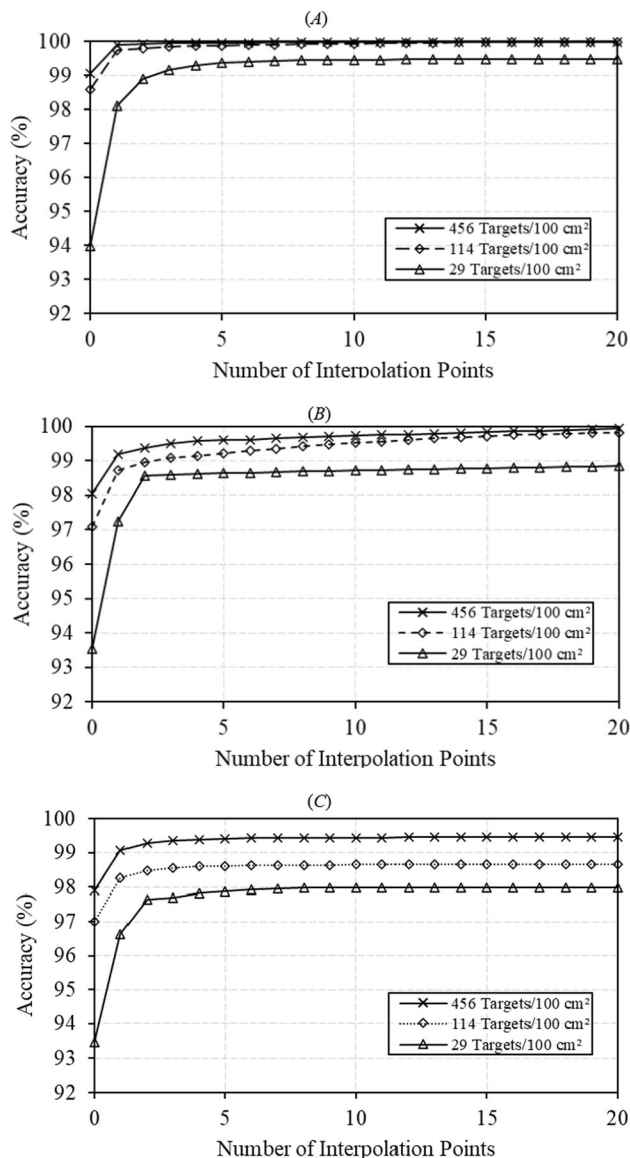
Fig. 12 Accuracy of volume calculation of the clay specimen at a different number of interpolation points at **a** 0% strain, **b** 9% strain, and **c** 15% strain

This is logical since the higher the number of targets used to represent the soil specimen, the higher the volume measurement accuracy is expected. Figure 11b shows the plots of volume measurement accuracy versus interpolation points at 9% strain considering different point densities. It can be noticed that all curves showed a similar trend. At this strain level, the soil specimen has been deformed as shown in Fig. 5b with a volume of $6.098*10^2$ cm^3 (Fig. 10a) and does not have a cylindrical shape. As for using 29 targets/100 cm^2 on the membrane surface area, the volume measurement accuracy can never reach an accuracy higher than 99% even by using a high number of interpolation points. Still, by using 144 targets/100 cm^2 or 456 targets/100 cm^2 on the membrane surface area, the

volume measurement accuracy cannot reach 100% even with a high number of interpolation points. Eventually, all results at 9% strain showed lower accuracy than those at 0% strain though more interpolation points are used. The reason for this is that the sand specimen has largely deformed at 9% strain in comparison with 0% strain. For Fig. 11c, the results are shown at 15% strain which is corresponding to Fig. 5c. At 15% strain, the sand specimen has very high deformation relative to bulging failure with a volume of $6.247*10^2$ cm^3 (Fig. 10a). It is noticed that the accuracy at 29 targets/100 cm^2 increased significantly from 92 to 96.5% even after applying the interpolation method with one interpolation point. The volume measurement accuracy has also increased with the number of interpolation points to reach a steady slope of values of 98 and 99.5% for 144 targets/100 cm^2 and 456 targets/ 100 cm^2, respectively. By comparing these results in Fig. 11b, c, the accuracy values at 15% are lower than those at 9% strain due to larger specimen deformation.

As for the clay specimen, the results of the volume measurement accuracy at different interpolations with various target densities are shown in Fig. 12a–c at 0, 9, and 15% strains, respectively. In Fig. 12a, the specimen has an imperfect cylindrical shape as shown in Fig. 5d with a volume of $5.552*10^2$ cm^3 (Fig. 10b). For all point densities, the volume measurement accuracy cannot reach higher than 99% after applying interpolation. Figure 12b shows the results of volume measurement at 9% strain which are corresponding to the slightly deformed cylindrical specimen shown in Fig. 5e. At this strain level, the clay specimen has a volume of $5.725*10^2$ cm^3 (Fig. 10b). Using 29 targets/100 cm^2 on the membrane surface area shows an initial accuracy of 93.5% with a dramatic increase after applying interpolation until reaching a gentle slope after three interpolation points. By using 114 targets/ 100 cm^2, the accuracy can reach 99.4% after 14 interpolation points. By using 456 targets/100 cm^2, the accuracy can reach a volume measurement accuracy higher than 99% after one interpolation point. At 15% strain, the results are shown in Fig. 12c where the specimen shows localized failure mode by shear band formation as presented in Fig. 5f. At this strain level, the clay specimen has a volume of $5.941*10^2$ cm^3 (Fig. 10b). The volume measurement accuracy for different target densities has increased with a higher number of interpolation points. An accuracy of 99.3% was achieved after 4 interpolation points by using 456 targets/100 cm^2. An accuracy of 98.5% was achieved after 5 interpolation points by using 114 targets/100 cm^2. As for 29 targets/100 cm^2, the accuracy reached 97.6% after 7 interpolation points. By comparing Figs. 11 and 12, it can be noticed that the overall volume measurement accuracy was higher for the clay specimen in comparison with the sand specimen. Also, fewer interpolation points

are required to reach a steady volume measurement accuracy for the clay specimen in comparison with the sand specimen. This is directly related to the deformation and failure mode difference between the clay and sand specimens. The sand with silt specimen showed more irregular and larger deformation during shearing at different strain levels in comparison with the clay specimen. Also, the sand specimen showed a bulging failure in comparison with the shear band formation failure for the clay specimen. Particularly, the deformation and failure mode of the sand with silt specimen, compared to the clay specimen, had a higher deviation from a cylindrical shape. In general, a higher target density is needed for larger and irregular deformation of the soil specimen. Similarly, a higher target density is required for soil specimens with expected bulging failure in comparison with soil specimens with expected shear band formation failure.

For both specimens, a common trend was noticed that a higher density of points and more interpolation points are needed at larger deformation to achieve high-volume measurement accuracy. Even by using interpolation, the volume measurement accuracy of a specimen represented by a low target density will not reach a very high value. Overall, applying interpolation can highly increase the volume measurement accuracy specifically for low target density. However, the interpolation can increase the volume measurement accuracy to a certain limit where the accuracy becomes steady after increasing the number of interpolation points. It can be also noticed that the effect of interpolation is related to the level and shape of deformation. Fewer interpolation points are needed at a lower strain level for specimens with shear band deformation. This is reasonable since the proposed interpolation method considers the cylindrical shape of the specimen. So that, in case the deformation is close to the assumption, then the results are better. When the assumption and the actual deformation do not match, the results become less accurate. At all strain levels, it can be noticed that increasing the density of targets rises the volume measurement accuracy. Also, increasing the number of interpolation points can increase the accuracy to a certain level. Based on the strain level, high accuracy can be achieved for different targets' densities. As deformation becomes larger, the maximum accuracy value decreases then a higher density of targets is required. However, the density of targets cannot be unlimitedly increased considering the target size and the processing time. So, it is better to choose the density of targets depending on the accuracy requirement, the maximum soil deformation level, and the expected failure mode of the specimen. To reach a volume measurement accuracy of 99.5%, for a relatively undeformed cylindrical shape of soil specimen at 0% strain, the required target density is at least 29 targets/100 cm^2 with the requirement of surface interpolation. However, at a higher strain level, even by using large interpolation points, a maximum accuracy level higher than 99.5% cannot be reached. So that to achieve volume measurement accuracy of 99.5%, the required target density increases to an optimum of 114 targets/100 cm^2 and 456 targets/100 cm^2 on the membrane surface at 9 and 15% strain, respectively, with the necessity to apply surface interpolation.

5 Conclusions

Discrete measurement targets have been broadly used in many image-based methods to monitor soil specimens during triaxial testing. However, the optimum target density needed during triaxial testing has never been investigated. It would be a valuable contribution to the literature and for researchers, to help them make decisions on the required optimum target density to achieve the desired level of volume measurement accuracy. In this study, the required target density on the specimen's surface is investigated to provide general guidelines for image-based methods using triaxial testing. A LiDAR scanner was used to determine the reference volume of the specimen. Since LiDAR scanning cannot be applied directly to triaxial soil specimens in confining fluid, unconfining compression tests were performed to mimic the soil specimen deformation during the triaxial testing. Different target densities of 29 targets/100 cm^2, 114 targets/100 cm^2, and 456 targets/100 cm^2 were used to represent the specimen. The testing was performed at different strain levels for two specimens of sand with silt and clay to consider the effect of deformation shape and failure mode on the calculated accuracy. The soil specimens have a diameter of 71 mm and a height of 140 mm. An interpolation method was proposed and used during testing by applying a different number of interpolation points. The results show that a higher target density is required at a larger strain. This is logical since the deformation can alter the initially cylindrical shape of the specimen so that more targets are needed to better represent the specimen and achieve high-volume measurement. In addition, the comparisons between the volume measurement results for each of the clay and sand with silt specimens emphasize the influence of deformation and failure mode on the requirement of target density. For larger and irregular deformation of the soil specimen, higher target density is needed. Correspondingly, a higher target density is required for soil specimens with expected bulging failure in comparison with soil specimens with expected shear band formation failure. Also, fewer interpolation points were needed for the clay specimen in comparison with the sand with silt specimen to reach maximum accuracy. For a relatively undeformed

cylindrical shape of soil specimen at 0% strain, the required target density is at least 29 targets/100 cm^2 with the requirement of 6 and 4 interpolation points for sand with silt and clay specimens, respectively, to reach a volume measurement accuracy of 99.5%. To achieve the same accuracy value, the required target density increases to an optimum of 114 targets/100 cm^2 by using 8 and 6 interpolation points for sand and clay specimens, respectively, at 9% strain. As for 15% strain, an optimum of 456 targets/100 cm^2 is needed by using 16 and 10 interpolation points for sand and clay specimens, respectively. It is worth noting that the conclusion derived from this research highlights the importance of the point density on the accuracy of the volume measurement; however, the accuracy of the 3D position of each individual point is also of much greater importance for an accurate volume measurement for image-based methods used in triaxial testing.

References

1. Alshibli KA, Sture S (1999) Sand shear band thickness measurements by digital imaging techniques. J Comput Civil Eng 13(2):103–109. https://doi.org/10.1061/(ASCE)0887-3801(1999)13:2(103)

2. Alshibli KA, Al-Hamdan MZ (2001) Estimating volume change of triaxial soil specimens from planar images. Comput-Aided Civ Infrastruct Eng 16(6):415–421. https://doi.org/10.1111/0885-9507.00243

3. Bhandari AR, Powrie W, Harkness RM (2012) A digital image-based deformation measurement system for triaxial tests. Geotech Test J 35(2):1–18. https://doi.org/10.1520/GTJ103821

4. Fayek S, Xia X, Li L, Zhang X (2020) Photogrammetry-based method to determine the absolute volume of soil specimen during triaxial testing. Transp Res Rec 2674(8):206–218. https://doi.org/10.1177/0361198120928339

5. Fayek S, Zhang X, Galinmoghadam J, Xia X (2022a) Evaluating the effects of specimen misalignment during triaxial testing using a photogrammetry-based method. IEEE Trans Intell Transp Syst. (Under Review)

6. Fayek S, Xia X, Zhang X (2022b) Consideration of one camera photogrammetry-based method to reevaluate some aspects of conventional triaxial methods. Paper presented at the Proceedings of the Geo-Congress: State of the Art & Practice in Geotechnical Engineering, Charlotte, North Carolina March 20–23, 2022. American Society of Civil Engineers (Tentatively Accepted)

7. Fayek S, Xia X, Zhang X (2022c) Validation of photogrammetry-based method to determine the absolute volume of unsaturated soils. Paper presented at Advances in Transportation Geotechnics IV, Lecture Notes in Civil Engineering 165, pp. 773–781, Springer, Cham. https://doi.org/10.1007/978-3-030-77234-5_63

8. Gachet P, Geiser F, Laloui L, Vulliet L (2007) Automated digital image processing for volume change measurement in triaxial cells. Geotech Test J 30(2):98–103. https://doi.org/10.1520/GTJ100309

9. Gesch KR, Wells RR, Cruse RM, Momm HG, Dabney SM (2015) Quantifying uncertainty of measuring gully morphological evolution with close-range digital photogrammetry. Soil Sci Soc Am J 79(2):650–659. https://doi.org/10.2136/sssaj2014.10.0396

10. Gordon S, Lichti D, Stewart M (2001) Application of a high-resolution, ground-based laser scanner for deformation measurements. Paper presented in Proceedings of 10th International FIG Symposium on Deformation Measurements, pp. 23–32

11. Kikkawa N, Nakata Y, Hyodo M, Murata H, Nishio S (2006) Three-dimensional measurement of local strain using digital stereo photogrammetry in the triaxial test. In: Hyodo M, Murata H, Nakata Y (eds) Geomechanics and geotechnics of particulate media. Taylor and Francis, London, pp 61–67

12. Li L, Li P, Cai Y, Lu Y (2021) Visualization of non-uniform soil deformation during triaxial testing. Acta Geotech 16:3439–3454. https://doi.org/10.1007/s11440-021-01310-w

13. Lin H, Penumadu D (2006) Strain localization in combined axial-torsional testing on kaolin clay. J Eng Mech 132(5):555–564. https://doi.org/10.1061/(ASCE)0733-9399(2006)132:5(555)

14. Macari EJ, Parker JK, Costes NC (1997) Measurement of volume changes in triaxial tests using digital imaging techniques. Geotech Test J 20(1):103–109. https://doi.org/10.1520/GTJ11424J

15. Parker JK (1987) Image processing and analysis for the mechanics of granular materials experiment. In: ASME proceedings of the 19th SE symposium on system theory, Nashville, TN, March 2, 1987, ASME, New York

16. Quinsat Y (2015) Filling holes in digitized point cloud using a morphing-based approach to preserve volume characteristics. Int J Adv Manuf Syst 81(1):411–421. https://doi.org/10.1007/s00170-015-7185-0

17. Rechenmacher AL (2006) Grain-scale processes governing shear band initiation and evolution in sands. J Mech Phys Solids 54(1):22–45. https://doi.org/10.1016/j.jmps.2005.08.009

18. Rechenmacher AL, Medina-Cetina Z (2007) Calibration of soil constitutive models with spatially varying parameters. J Geotech Geoenviron Eng 133(12):1567–1576. https://doi.org/10.1061/(ASCE)1090-0241(2007)133:12(1567)

19. Sachan A, Penumadu D (2007) Strain localization in solid cylindrical clay specimens using digital image analysis (DIA) technique. Soils Found 47(1):67–78. https://doi.org/10.3208/sandf.47.67

20. Salazar SE, Coffman RA (2015) Consideration of internal board camera optics for triaxial testing applications. Geotech Test J 38(1):40–49. https://doi.org/10.1520/GTJ20140163.ISSN0149-6115

21. Salazar SE, Coffman RA (2015) Discussion of 'a photogrammetry-based method to measure total and local volume changes of unsaturated soils during triaxial testing' by Zhang et al. Acta Geotech 10(5):693–696. https://doi.org/10.1007/s11440-015-0380-1

22. Uchaipichat A, Khalili N, Zargarbashi S (2011) A temperature controlled triaxial apparatus for testing unsaturated soils. Geotech Test J 34(5):424–432. https://doi.org/10.1520/GTJ103586

23. White DJ, Take WA, Bolton MD (2003) Soil deformation measurement using particle image velocimetry (PIV) and photogrammetry. Géotechnique 53(7):619–632. https://doi.org/10.1680/geot.2003.53.7.619

24. Xia X, Zhang X, Fayek S, Yin Z (2021) A table method for decoding of coded target decoding with application to three-dimensional 3D reconstruction measurement of soil samples during triaxial testing. Acta Geotech 16(12):1–13. https://doi.org/10.1007/s11440-021-01343-1

25. Yang F, Su D, Ma Y, Feng C, Yang A, Wang M (2017) Refraction correction of airborne LiDAR bathymetry based on sea surface profile and ray tracing. IEEE Trans Geosci Remote Sens 55(11):6141–6149. https://doi.org/10.1109/TGRS.2017.2721442

26. Zhang X, Li L, Chen G, Lytton R (2015) A photogrammetry-based method to measure total and local volume changes of

unsaturated soils during triaxial testing. Acta Geotech 10(1):55–82. https://doi.org/10.1007/s11440-014-0346-8

27. Zhao C, Koseki J (2020) An image-based method for evaluating local deformations of saturated sand in undrained torsional shear tests. Soils Found 60(3):608–620. https://doi.org/10.1016/j.sandf.2020.02.012